LPO DEVELOPMENT IN LINEATED PERIDOTITES


A Thesis

by

LINDSEY YORKE GERMAN



Submitted to the Office of Graduate and Professional Studies of
Texas A&M University
in partial fulfillment of the requirements for the degree of

MASTER OF SCIENCE



| | |
|---|---|
| Chair of Committee, | Julie Newman |
| Committee Members, | Will Lamb |
| | Deborah Thomas |
| Head of Department, | Michael Pope |


May 2016


Major Subject: Geology

ABSTRACT


Lattice preferred orientation (LPO) in olivine-rich rocks reflects deformation conditions and kinematics in the Earth's mantle. Harzburgites with a strong lineation and weak foliation have recently been identified in the eastern part of the Red Hills massif in the Dun Mountain Ophiolite Belt in New Zealand. While studies have characterized the LPO in lineated rocks for minerals such as pyroxene and quartz subjected to constrictional strain, little work has focused on characterizing the crystallographic - preferred orientation of olivine in lineated peridotites. Microstructural data and fabric geometry suggest that spinel does not reflect the strain experienced by the rock as a whole, in spite of being used as an indicator for the average foliation and lineation. Additionally, this study supports existing work involving the relationship between the development of LPO and rotation of crystallographic axes in response to the principal stretches of the finite strain ellipsoid. The data suggest the pencil glide system can be activated not only in response to experimentally determined strain rates and temperatures, but also in response to the rotation of the principal stretches of the finite strain ellipsoid.

# NOMENCLATURE

RHUM            Red Hills Ultramafic Massif

LPO             Lattice Preferred Orientation

SPO             Shape Preferred Orientation

SEM             Scanning Electron Microscopy

TEM             Transmission Electron Microscopy

EBSD            Electron Backscatter Diffraction

X-ray CT        X-Ray Computed Tomography

TABLE OF CONTENTS

# 1.  INTRODUCTION


Lattice preferred orientation (LPO) of naturally deformed rocks forms under a range of conditions, and occurs in response to slip on specific crystallographic planes that are activated under a unique set of conditions. Thus, analysis of these textures (LPOs) for a particular mineral yields constraints on deformation conditions including water content, stress, strain rate, temperature, pressure and strain as well as kinematics (e.g., Flinn, 1965; Katayama et al., 2004; Sullivan et al., 2010). Olivine rheology has been well characterized through rock deformation experiments, and the LPO of olivine deformed primarily under simple-shear conditions has been the focus of many studies (Hirth and Kohlstedt, 2003; Katayama et al. 2004; Jung et al., 2006). In general, olivine in the upper mantle deforms by dislocation creep, a mechanism that involves development of a LPO. Five main LPO types have been identified through investigation of experimentally deformed samples and each is well characterized for a range of conditions. The two most common textures observed in both naturally and experimentally deformed rocks are the A and D types (Jung et al., 2006; Karato et al., 2008; Kaplanis et al., 2013; Hansen et al., 2014). The A type slip system (001)[100], is dominant under high temperature, dry, and low flow stress conditions, and the D type slip system (0kl)[100], also known as pencil glide, occurs under dry conditions, lower temperatures and higher flow stresses (Zhang and Karato, 1995; Zhang et al., 2000). The remaining B, C, and E types are less common and dominate under a range of conditions of water content, temperatures, and flow stresses.

1

However, the development of LPO may not depend solely on the previously mentioned deformation conditions. This statement is well supported in studies involving the development of a preferred orientation in response to fabric geometry (3D grain shape) in crustal material (Schmid and Casey, 1986; Lloyd et al., 2011; Llana-Funez and Rutter, 2014), but this relationship is poorly constrained for minerals common in the upper mantle. However, previous work may suggest a significant link between LPO formation and fabric geometry for olivine in the upper mantle. For example, a compression experiment for olivine over a range of deformation conditions was not able to produce the D-type pattern in olivine (Ave'Lallemant and Carter, 1970). Furthermore, some studies record the existence of the D-type pattern in association with torsion experiments (Bystricky et al., 2000; Hansen et al., 2014). Additionally, previous work records the existence of the B-type olivine fabric in response to a kinematic effect due to strain partitioning during melt segregation (Hotlzman et al., 2003). The development of the B-type fabric has also been attributed to pure shear dominated deformation and elongation normal to the shear direction (Karato et al., 2008). Thus, these studies support a clear relationship between fabric geometry and the development of a LPO in olivine.

L-tectonites, or rocks with a dominantly linear fabric, have been extensively studied for naturally and experimentally deformed quartz-rich rocks, and these fabrics are generally considered to develop as a result of constrictional strain, forming distinct crystallographic fabrics (Flinn, 1965; Tullis, 1977; Lister and Hobbs, 1980; Sullivan et al., 2010). This strong, linear alignment of minerals with a weak or nonexistent foliation is not common in the literature (Pfiffner and Ramsay, 1982), and knowledge concerning

the tectonic evolution of large domains of L tectonites is lacking, largely due to the difficulty in understanding the complicated, polyphase deformational histories of the associated areas (Sullivan, 2013). However, constrictional deformation is a significant structural feature in various geologic settings around the world and should not be ignored (e.g., Holst and Fossen, 1987; Sylvester and Janecky, 1988; Poli and Oliver, 2001; Solar and Brown, 2001; Sullivan, 2013).

Recent fieldwork in the Red Hills massif has identified olivine-rich rocks with a linear fabric. Analysis of these fairly unexplored fabrics in olivine-rich rocks will improve our understanding of the deformation mechanisms and lattice preferred orientations associated with the development of L-tectonites in peridotites. In studies of naturally deformed peridotites, mantle massifs and xenoliths, the geometry of spinel grains are assumed to reflect the kinematic geometry of the rocks (e.g., Michibayashi et al., 2006); the geometry of spinel grains are used to define the orientation context (foliation and lineation) within which other data, such as LPO, are viewed. The linear fabric in these rocks, not typical of most reported studies of naturally deformed peridotites, offers a new context within which to evaluate the use of spinels for this purpose.

By using a combination of methods involving X-ray CT analysis coupled with microstructural work involving analysis of LPO, and grain shape analysis on two mutually perpendicular thin sections, this study: 1) discusses the use of the X-ray CT in peridotites; 2) examines the relationship between fabric geometry and the development of LPO; and 3) compares the development of olivine and spinel fabric in peridotites.

3

The results of this study suggest that while spinel grains are typically used to identify foliations and lineations in peridotites, this mineral does not necessarily reflect the complete strain experienced by the rock; olivine fabrics and spinel fabrics do not reflect the same strain at the deformation conditions experienced by these Red Hills peridotites. Further, LPO in olivine appears to be controlled by the development of the constrictional fabric, rather than deformation conditions alone. This result supports the relationship documented in previous studies investigating LPO development in response to a kinematic framework (e.g., Ribe and Yu, 1991; Tommasi et al., 1999; Miyazaki et al., 2013; Chatzaras and Kruckenberg, in review).

## 2. GEOLOGIC SETTING

The peridotites described in this study are from the Red Hills ultramafic massif (RHUM), part of the Permian Dun Mountain Ophiolite Belt in New Zealand (Figure 1a). This massif is the largest in the belt with an area spanning 12 km by 8 km, and has been extensively mapped by Walcott (1969), Johnston (1982), Johnston (1990) and Stewart (2015). Previous work involving clinopyroxene rare earth element patterns by Sano and Kimura (2007) links the ultramafic complex to a paleo-mid ocean ridge setting, but more recent geochemical work and extensive mapping by Stewart (2015) suggests the complex may have developed during an early stage of subduction.

Based on lithology and mesoscale fabrics, Stewart (2015) divides the RHUM into four distinct units (Figure 1): From west to east, these are the Ellis Stream Complex, the Plateau complex, the Plagioclase zone, and the Two Tarns harzburgite. The massif likely experienced two stages of melting involving metasomatism and melting of refractory mantle (Sano and Kimura, 2007, Stewart, 2015). Microstructural analysis and field work by Stewart (2015) suggests the Two Tarns harzburgite represents an early stage of melting and denotes refractory mantle, and a later stage of refertilization is responsible for producing the other ultramafic bodies within the massif: the Plateau complex, the Plagioclase zone, and the Ellis Stream complex. The Plateau complex is comprised of banded harzburgite and dunite, while rocks in the Plagioclase zone are discontinuous lenses and sills of foliated plagioclase lherzolite and plagioclase harzburgite. The Ellis Steam Complex is comprised of compositionally banded

harzburgite and dunite with minor lherzolite and a strong planar fabric. More dunite is recognized in the Ellis Stream complex than the Plateau complex.  Although the later episode of metasomatism is focused in the western massif, it is present throughout the Red Hills at various scales.

The olivine-rich rocks focused on in this study are from the Two Tarns harzburgite. Geothermobarometric analyses suggest these rocks formed at approximately 1200°C and > 6 kbar pressure (Stewart, 2015). Orientation information collected in the field by Stewart (2015) is recorded in Figure 2. At the mesoscale, the harzburgites appear mostly massive with a linear fabric defined by spinel geometry. Foliation in these rocks is weakly developed, with the poles forming a girdle dipping to the west. In some outcrops, foliation is not observable and is not recorded.

# 3. METHODS

## 3.1 X-ray Computed Tomography

Foliation is difficult to discern in mesoscale exposures and hand samples from the Two Tarns Harzburgites (Stewart 2015). Therefore, fabric information was obtained using X-ray CT scans (Department of Earth Sciences, The University of Minnesota; X5000 high resolution microCT with a dual head 225 keV cone-beam X-ray source coupled with a Dexela area detector). X-ray CT produces tomographic images (slices) of rock and provides fabric information in 3D. In these harzburgites, spinel grains were analyzed using the X-ray CT because the mineral's higher density and atomic number results in attenuation of more X-rays than other phases in the rock. The X-ray CT identifies the foliation plane (XY) and the XZ plane (Figure 3), based on the average of spinel grain geometries in each sample; the intersection between these two planes defines the mineral stretching lineation orientation. Nine olivine-rich samples (10 x 5 x 3 cm) from the Red Hills were scanned, reconstructed, and analyzed to determine spinel fabric geometry. This geometry was used to define foliation and lineation in each sample. In order to determine dependency of fabric geometry on sample size, two samples were cut to 2 x 4 x 1 cm billets and reanalyzed using the X-ray CT: 14RH-07 and 14RH-13. The X-ray CT also provided grain size data for all spinel grains. The software assumes a spinel's grain size is equivalent to the length of a cube whose volume equals that of a spinel grain.

7

3.2 Microstructural Analysis

Nine thin sections were prepared parallel to the lineation and perpendicular to foliation as defined by the X-ray CT. In addition, thin sections parallel to both the foliation and lineation were prepared for seven of the nine samples. Thin sections oriented parallel to lineation and perpendicular to foliation were analyzed using a Tescan Vega 3 LMU scanning electron microscope (SEM) and Oxford Instruments Nordyls Max2 electron backscattered diffraction (EBSD) at Boston College, at 25 kV and 50 nA beam current; EBSD maps were created with a step size of 7.5 microns. Modal mineralogy, grain size and shape preferred orientation were determined from EBSD map data for these samples, using Oxford Instruments AZtecHKL Channel 5 software.

In addition, for the seven samples for which thin sections were prepared parallel to both the foliation and lineation, grain size analyses were carried out using image processing software (Image SXM, Barrett (2008)) on grain traces from optical photomicrographs of thin sections from the two mutually perpendicular thin sections: (1) parallel to lineation and perpendicular to foliation and (2) parallel to lineation and foliation. For shape analysis, the software assumes an ellipse for grains, and determines the length of long and short axes, as well as the orientation of the long axes for each grain. This analysis was carried out only for olivine grains, due to the limited amount of spinel and other phases observable in thin section.

Backscattered electron imaging (BSE) on the electron microprobe at Texas A&M was also used to investigate microstructures at a scale below resolution of the optical microscope.

# 4. RESULTS

## 4.1 Fabric Analysis

Spinel geometries determined through X-ray CT analyses suggest lineations and foliations consistent with those collected by Stewart (2015) in the field (Figure 2). Spinel lineations are consistent, with an average orientation of 30º at 101. However, highly variable foliation is recorded from both field observations and X-ray CT.

X-ray CT data suggest variable strain geometries for spinel grains (Figure 4). Four samples (14RH-11, 14RH-02, 14RH-02b, 14RH-10) from the Red Hills record prolate fabric ellipsoids ($S_1>S_2\approx S3$, where $S_1$, $S_2$, $S_3$ are the maximum, intermediate, and minimum stretches) and 5 samples (14RH-03a, 14RH-14, 14RH-13, 14RH-12, 14RH-7) fall in the flattening field with oblate fabric ellipsoids ($S_1\approx S_2>S_3$).

Reanalysis of two samples using smaller sample sizes indicates that the resolution of the analyses is related to the size of the samples; for the larger samples (average size: 10 x 5 x 3 cm) analyzed, spinel grains > ~300 μm are resolved. Two samples (14RH-07 and 14RH-13) that record oblate fabrics from large samples were reanalyzed using a smaller sample size (average size: 2 x 4 x 1 cm) (Figure 5). Analyses of the smaller samples allow for resolution of finer-grained spinel (>100 μm). The reanalysis of the smaller samples suggest more prolate geometries for both samples (Figure 4). While the large sample analyzed for 14RH-07 indicates an oblate geometry, reanalysis as a smaller sample suggested an overall prolate fabric geometry. When Sample 14RH-13 was reanalyzed as a smaller sample, the fabric geometry for spinel

became less oblate as well, but the results did not significantly change from those derived from the analysis on the larger sample.

The Lode's ratio (v) is a function of the principal stretching axes and is used to characterize fabric geometry (Ramsay and Huber, 1983). It is determined using the following equation:

$$v = \frac{2(\ln(S1) - \ln(S3))}{\ln(S1) - \ln(S3)} \qquad (1)$$

where $S_1$ and $S_3$ are the maximum and minimum principal stretches, respectively. The Lode's ratio falls between -1 and 1, where v<0 describes prolate ellipsoids, v=0 denotes plain strain, and v>0 refers to oblate ellipsoids. The Lode's parameter for each individual spinel grain analyzed by the X-ray CT is presented in Figure 5. The average spinel grains size is between 100 and 500 um and there is no clear relationship between fabric geometry and spinel grain size within any given sample, including both the larger and smaller samples. However, when grain size is viewed as two populations: (1) all grains less than 1000 μm, and (2) all grains greater than 1000 μm (Figure 6), the coarser grain populations tend to be more prolate compared to the finer grain populations (for six out of nine samples: 14RH10, 14RH03a, 14RH14, 14RH13, 14RH12, 14RH07.)

Strain ellipsoid values for olivine derived from Image SXM analyses are presented in Figure 4. For this analysis carried out using photomicrographs taken on an optical microscope, a resolution of 60 μm was achieved. Six out of the seven samples analyzed record prolate fabrics for olivine. Spinel fabric analyses derived from the X-ray CT are overlain for comparison (Figure 4). Four out of the six samples that yield prolate values for olivine, indicate oblate values for spinel based on X-ray CT analyses (14RH-

10

03a, 14RH-12, 14RH-14, 14RH-13). Samples 14RH-11 and 14RH-10 yield prolate shapes from both olivine and spinel analysis, and the olivine analyzed from sample 14RH-02b records oblate shapes while the spinel for this sample is characterized as prolate. Note that sample 14RH-02b, the only sample that records oblate fabric for olivine, is part of a folded pyroxene band.

4.2 Microstructural Analysis

The Two Tarns harzburgites consist of olivine and orthopyroxene with clinopyroxene, hornblende, and spinel (Table 1.) All thin sections show some degree of serpentinization, although typically < 5%. Grain size distributions for olivine (Figure 7) vary from sample to sample, with a range in grain size from 30 to 5000 μm (minimum grain diameter reported is 30 μm due to resolution of the EBSD analyses). The coarse grain size populations of orthopyroxene, olivine, and clinopyroxene range in size from 1000 to 5000 μm (Figure 8A). These larger orthopyroxene grains often contain exsolution lamellae of clinopyroxene (Figure 8B) and coarse olivine grains show well-developed subgrains and undulatory extinction (Figure 8A, C).

Three samples (14RH-02, 14RH-13, and 14RH-14) show, locally, a fine-grained (15 μm <150 μm), polymineralic matrix (Figure 8C, D). These fine-grains are comprised of olivine, orthopyroxene, clinopyroxene and spinel and are often located adjacent to larger grains with irregular, sometimes curved grain boundaries. Fine-grained zones locally align grain boundaries between coarser grains (Figure 8C, D). Coarse olivine grains are often located near other olivine grains of similar size and orientation, separated by fine-grained material with variable compositions (Figure 8C). Large

orthopyroxene grains are occasionally surrounded by finer-grained olivine and orthopyroxene (Figure 8E). Fine-grained orthopyroxene (Figure 8H) and spinel (Figure 8C, D) locally surround larger olivine grains. Clinopyroxene grains are frequently surrounded by a finer grained matrix of clinopyroxene and olivine (Figure 8G). Spinel grains (~500 μm) often have curved and irregular grain boundaries (Figure 8F).

The mean spinel orientation derived from the X-ray CT (labeled $L_1$ in Figure 9) is defined as the average orientation of all spinel long axes. However, within a sample, spinel orientations are highly variable (Figure 9). Olivine grains, in all samples, exhibit a strong SPO parallel or subparallel to the average lineation defined by X-ray CT analyses of spinel.

Spinel grains do not record a LPO (Figure 9) and misorientation within a single grain is below one degree (Figure 10). Olivine in all samples are characterized by [100] maxima parallel or subparallel to the lineation; [010] and [001] produce girdles perpendicular to the foliation, consistent with D-type (pencil glide) LPO for olivine (Figure 9; Jung et al., 2006; Karato et al., 2008; Kaplanis et al., 2013; Hansen et al., 2014). Because of the heterogeneous grain size distributions, we investigated LPO in different grain size populations for all samples and the LPO does not vary with grain size (e.g., Figure 11).

# 5. DISCUSSION

## 5.1 Melt-Related Deformation and Deformation Mechanisms

Samples are composed predominantly of coarse-grained (1000 µm to 5000 µm) olivine with orthopyroxene and less commonly clinopyroxene and spinel. However, fine-grained (15 µm to 150 µm) polyphase material comprised of olivine, clinopyroxene, orthopyroxene and spinel (Figure 8C, D, E, G, H) is present locally in three thin sections. These fine grains are commonly found at the boundaries of larger grains that often exhibit irregular or curved boundaries (Figure 8F), suggesting they formed by reaction in the presence of melt (Stewart 2015). Preservation of the melt-related microstructures suggests that the associated event occurred later or at the same time as sub-solidus deformation. The fine-grained clinopyroxene surrounded by olivine (Figure 8D, G) suggests incomplete melting and partial dissolution of the larger clinopyroxene grains (Niu, 1997), and the fine-grained matrix comprised of orthopyroxene and olivine surrounding larger orthopyroxene grains (Figure 8E) may have developed in response to the following reaction:

$$orthopyroxene + low\ silica\ melt\ \rightarrow olivine + high\ silica\ melt \quad (1)$$
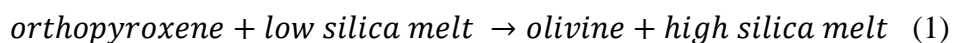
The larger orthopyroxene grains experienced incomplete dissolution or melting, with the smaller orthopyroxene grains representing portions of unmelted material (Niu, 1997). However, the finer grained orthopyroxene is also found in contact with larger olivine grains (Figure 8H) and may result from the following reaction where olivine reacts with a high silica melt to form orthopyroxene (Soustelle et al., 2010):

13

$$olivine + high\ silica\ melt \rightarrow orthopyroxene + low\ silica\ melt \quad (2)$$

Fine-grained spinel (<150 µm) in the melt-related matrix (Figure 8D) and coarser grained spinels (~500 um) with curved grain boundaries (Figure 8F) suggests that melt-related events may have also had a local influence on this mineral (Soustelle et al., 2010). These irregular grain shapes indicate that spinel grains likely formed in the presence of melt.  It is not, however, clear from the current data what deformation mechanism dominated their deformation. In contrast, undulatory extinction, subgrains, shape preferred orientation, and the presence of a LPO for olivine grains suggest deformation by dislocation creep (Figures 8 and 9) (Passchier and Trouw, 2005), and the absence of a LPO combined with no significant internal deformation in spinel (Figure 9,10) suggests that dislocation motion was not the dominant deformation mechanism in spinel grains. However, transmission electron microscopy (TEM) analysis on spinel grains would provide more data on evidence for dislocation creep.

5.2 Prolate vs. Oblate Fabrics

Fabric analyses of spinels using X-ray CT indicate four samples with prolate fabric ellipsoids and five samples with oblate fabric ellipsoids (Figure 4). However, reanalysis of two samples using smaller samples yield more prolate fabrics than indicated by analyses of the larger samples, suggesting Lode's parameter may be strongly dependent on sample size (Figure 6). As the sample size decreased, X-ray CT analysis was able to resolve smaller grains.  For example, in sample 14RH-07, the minimum spinel grain size analyzed changed from 300 µm to 100 µm for larger and smaller samples, respectively, suggesting either that the smaller grains (between 100 µm

14

and 300 μm) yield more prolate geometries, or, that the sample size influences the results for all grains. Plots of grain size vs. Lode's parameter (Figure 5 and 6) do not suggest that smaller grains are more prolate. Additional analyses are necessary to resolve this question. It is important to note that while spinel grains show a range of geometries and shape preferred orientations (Figure 9), olivine grains exhibit a strong SPO parallel or subparallel to the lineation determined from the X-ray CT analyses of spinel, as well as strong point maxima of [100] parallel or subparallel to lineation, indicating that the X-ray CT data were reliable for defining foliation and lineation in these rocks.

Fabric geometry of olivine grains, determined using Image SXM on grain traces from optical photomicrographs, suggests olivine grains have a stronger lineation than foliation, with the exception of one sample, 14RH-02b, which records oblate shapes (Figure 4). However, this sample is part of a folded pyroxene band (Stewart, 2015), which may have influenced its fabric.

5.3 Olivine vs Spinel Rheology

Spinel geometries derived from X-Ray CT analyses are variable, indicating both prolate and oblate elliposids (Figure 4). Variability in spinel fabric is also evident in its SPO, which differs from that of olivine (Figure 9). While olivine grains show a strong SPO parallel or subparallel to the lineation defined by the average spinel geometries, spinel grains do not show a strong shape preferred orientation, and only relatively few grains are oriented parallel to the average lineation derived by X-ray CT (Figure 9). In addition, no LPO is indicated for spinel grains, while olivine grains show a strong LPO, with [100] point maxima and [010] and [001] girdles perpendicular to the lineation

(Figure 9). These data suggest that while olivine deformed by dislocation creep, resulting in strong shape preferred orientations (Figure 9), spinel grains are not strongly deformed, and did not experience significant dislocation creep. However, the olivine LPO and SPO are consistent with the lineation and foliations as defined by spinel geometries, indicating that spinel grains did deform concurrently with the olivine, yet they do not record as strong a shape preferred orientation as olivine.

These LPO and SPO data for olivine and spinel, and the greater variability in spinel geometries (oblate to prolate geometries) relative to olivine (dominantly prolate) suggest that spinel is stronger than olivine at these deformation conditions. However, the deformation mechanism for spinel grains is not clear. It is possible that the finer grained spinel population, which tend to be more oblate than the coarser grained population (Figure 6), precipitated from melt, and thus, do not preserve the constrictional deformation seen in the older, larger grains. Coarser grains, in turn, may have deformed by limited dislocation activity, or stress-induced diffusion; compositional analysis could provide information on preferential chemical zoning in spinels (e.g., Ozawa, 1989). Further, preferential melt-rock reaction in a stress field may have influenced the shape of grains. Further analysis is necessary to determine whether spinel grain geometries formed from melt-rock reaction, precipitation from a melt, or from deformation (dislocation or diffusion) (Secher, 1981; Christiansen, 1985; Ozawa, 1989). Because internal deformation is not significant, it is possible that spinel may be deforming by passive rotation in a weaker matrix (Christiansen, 1985). This study would benefit from (1) transmission electron microscopy (TEM) to look for evidence of dislocations and (2)

compositional analyses on coarse vs. fine grains to look for zoning and evidence for diffusion.

5.4 Development of Lattice Preferred Orientation

Development of lattice preferred orientation is commonly attributed to deformation conditions such as stress, strain rate, temperature, and water content (e.g., Flinn, 1965; Katayama et al., 2004; Sullivan et al., 2010). As demonstrated in laboratory experiments, distinct LPOs are expected to form in response to these deformation conditions (e.g., Katayama et al., 2004; Jung et al., 2006). However, existing work also suggests that the kinematic context may play a significant role in LPO development (Bystricky et al 2000; Hansen et al., 2014).

The relationship between strain rate and stress for olivine is determined from the following flow law:

$$\blacktriangleright \quad \dot{\varepsilon} = A_d \frac{\sigma^n}{d^p} \exp\left[-\frac{Q+PV}{RT}\right]$$

(2)

where $\varepsilon$ is strain rate, $A_d$ is a material parameter, $\sigma$ is differential stress, n is a constant and its value depends on the dominant creep process, d is the grain size with exponent p, E* is activation energy, V is activation volume, Q is activation energy, P is pressure, R is the gas constant, and T is temperature (Kohlstedt et al., 1995; Mei and Kohlstedt, 2005). Using variables from Hirth and Kohlstedt (2003) and Hansen et al. (2011), two deformation mechanism maps for olivine are shown in Figure 12 (van der Wal et al., 1993). Based on geothermometry by Stewart (2015), deformation conditions are

17

estimated at 1200ºC and 600 MPa. The estimated differential stress is calculated using the following equation:

$$\sigma = (.015/D_g)^{1/1.33}$$

<div align="right">(3)</div>

where $D_g$ is the mean grain size of each olivine-rich rock and $\sigma$ is stress in MPa (van der Wal et al., 1993). The minimum grain size cutoff is <60 um, based on resolution of EBSD maps; this cutoff excludes fine grains formed by melt-related processes from the average grain size used for paleopiezometry. Stresses for these rocks range from 18 to 30 MPa (Figure 12). The flow law in equation 2 suggests these rocks formed at strain rates between $10^{-10}$ and $10^{-8}$ s$^{-1}$. Note that these strain rates are very fast. The deformation mechanism map created using variables from Hirth and Kohlstedt (2003) suggests the rocks deformed by disclocation creep, which is consistent with the interpretation made from thin-section analysis. However, the deformation mechanism map created using variables from Hansen et al. (2011) suggests deformation involved grain boundary sliding accommodated by dislocation activity. It is possible that melt may have facilitated the GBS.

Furthermore, the observed D-type LPO (Figure 9, 10) is commonly associated with high stresses and low temperatures (~900ºC; Carter and Ave'Lallemant, 1970; Nicolas and Christensen, 1987), but geothermometry reported by Stewart (2015) suggests these Red Hills rocks formed at much higher temperatures (1200ºC) than are usually associated with pencil glide texture. Thus, there is not a clear relationship between LPO and deformation conditions in these rocks.

We propose an alternative interpretation for the observed LPO based on the relationship between olivine crystallographic axes and the orientation and magnitude of the finite strain ellipsoid (e.g., Ribe and Yu, 1991; Tommasi et al., 1999; Miyazaki et al., 2013; Chatzaras and Kruckenberg, in review). In Figure 9, olivine [100] develop a point maximum near the maximum principal strain axis (the lineation orientation), and the b- and c- axes form a girdle on the plane defined by the intermediate and minimum principal strain axes. In samples where the lineation is much stronger than the foliation, the intermediate and short finite strain axes are very close in value, often becoming interchangeable. Thus, the girdled pattern we see for [010] and [001] may have formed due to these axes becoming interchangeable during constrictional deformation. This relationship between three-dimensional deformation and LPO development supports the arguments made in Chatzaras and Kruckenberg (in review) based on their analyses of peridotite xenoliths from west Antarctica. The D-type olivine LPO recorded for all prolate peridotites from the Red Hills is similar to the LPOs associated with the west Antarctica samples that exhibit prolate spinel ellipsoids. Antarctica xenoliths with oblate spinels record the AG type LPO, and samples comprised of spinel shapes approximating plane strain exhibit the A-type LPO. Although the Red Hills rocks record a range of fabric geometries for spinel (Figure 4), most samples record prolate fabrics for olivine and the D-type olivine LPO is present in all samples. It is important to note that fabric analysis was limited to spinel in the Antarctica study; olivine and fabrics are not reported. Analysis of the Red Hills rocks records conflicting fabric geometries from the two minerals; the two minerals reflect different strain, although not different strain

19

orientations, suggesting that olivine deformed more easily at these conditions than spinel. Characterization of olivine fabrics in samples where spinel fabrics and olivine LPOs are variable, as in the Antarctica xenoliths, would improve our understanding of the development of olivine vs. spinel fabric geometry.

5.5 Tectonic Setting for the L Tectonites

The melt-related microstructures and well-developed olivine prolate fabrics of the Two Tarns harzburgites are consistent with the interpretation of Stewart (2015) that the harzburgites experienced oblique transtensional deformation during pervasive melting. Stewart (2015) suggests that the Two Tarns harzburgites developed during the first of three stages that affected the Red Hills rocks between 285 and 274 Ma. Subduction is thought to have initiated along a mid-ocean ridge transform fault, and Stage 1 is associated with homogenous and highly oblique transtensional deformation, consistent with the development of linear fabrics (Sullivan, 2013; Stewart, 2015). Stage 1 is also linked to the formation of homogenous and pervasive melts in response to decompression melting and volatiles (e.g. Shervais, 2001). The microstructures in these rocks suggest relatively low stresses and fast strain rates are associated with the constrictional deformation in the presence of melt at this stage. Continued subduction in Stage 2 increased the dip of the descending plate, causing dextral and normal motion. Further mantle upwelling transported melt into more focused and narrower channels at shallower depths, forming more compositionally heterogeneous units adjacent to the Two Tarns in the DMOB.

## 6. CONCLUSION

In lineated harzburgites from the Red Hills ultramafic massif, olivine and spinel preserve different microstructures, fabrics and LPOs. Olivine grains display evidence for dislocation creep, including subgrains, undulose extinction, a strong shape-preferred orientation, and lattice preferred orientations with [100] parallel to the lineation. Spinel exhibits weak to no shape preferred orientation nor LPO. Further, X-ray CT analyses for spinel indicate a range of oblate to prolate fabrics (L>S L=S and L<S ellipsoids), while olivine grains analyzed using Image SXM on traces of optical photomicrographs yield prolate fabrics (L<S tectonites). These texture and fabric data suggest that olivine deformed more easily at these conditions than spinel. The olivine SPO and LPO, however, are parallel or subparallel to the average lineation as defined by spinel geometries, indicating that spinel fabrics were formed concurrently with the olivine deformation. Evidence for melt during deformation, in the form of fine-grained polyphase material, including spinel, and spinel microstructures (e.g., irregular grain shapes; cuspate-lobate grain boundaries between olivine and pyroxenes), suggest that spinel geometries formed during melt migration concurrent with olivine deformation. Whether these spinel geometries formed by deformation (dislocation or diffusion creep), melt-rock reaction, passive rotation, or precipitation from a melt requires additional research.

Pencil-glide is typically associated with deformation at relatively lower temperatures and higher stresses than suggested by the compositions and microstructures

(e.g., grain size) in these rocks.  We propose an alternative explanation for the D-type LPO that considers the kinematic context of these rocks.   While L-tectonites in peridotites have only rarely been described, LPO development in other minerals have been tied to the development of prolate fabric geometries. In addition, these results are consistent with analyses of Chatzaras and Kruckenberg (in review) of peridotite xenoliths that ties the development of LPO to strain geometry; crystallographic axes rotate relative to the principal stretches of the strain ellipsoid.  We propose the pencil glide system can be activated not only in response to deformation conditions of stress, strain rate, and temperature, but in response to constrictional strain during the development of L-tectonites.

REFERENCES

Ave'Lallemant, H. G., and Carter, N. L., 1970, Syntectonic recrystallization of olivine
and modes of flow in the upper mantle: Geol. Soc. America Bull., v. 81, no. 8, p.
2203.

Barrett, S. D., 2008, Image SXM. http://www.ImageSXM.org.uk.

Bystricky, M., Heidelbach, F., and Mackwell, S., 2006, High shear strain of olivine
aggregates: rheological and seismic consequences: Science, v. 290, p. 1564-
1567.

Carter, N. L., and Ave'Lallemant, H. G., 1970, High Temperature Flow of Dunite and
Peridotite: Geological Society of America Bulletin, v. 81, no. 8, p. 2181-2202.

Chatzaras, V., and Kruckenberg, S., in review, Effect of strain geometry on mantle
fabric and olivine crystallographic texture.

Christiansen, F. G., 1985, Deformation fabric and microstructures in ophiolitic chromites
and host ultramafics, Sultanate of Oman: Geologische Rundschau, v. 74, p. 61-
76.

Flinn, D., 1965, On the symmetry principle and the deformation ellipsoid: Geological
Magazine, v. 102, no. 1, p. 36-45.

Gleason, G. C., Tullis, J., and Heidelbach, F., 1993, The role of dynamic
recrystallization in the development of lattice preferred orientations in
experimentally deformed quartz aggregates: Journal of Structural Geology, v. 15,
no. 9, p. 1145-1168.

Hansen, L. N., Zhao, Y.-H., Zimmerman, M. E., and Kohlstedt, D. L., 2014, Protracted fabric evolution in olivine: Implications for strain measurement and seismic anisotropy: Earth and Planetary Science Letters, v. 387, p. 157-168.

Hirth, G., and Kohlstedt, D. L., 2003, Rheology of the Upper Mantle and the Mantle Wedge: A View from the Experimentalists: Inside the Subduction Factory, v. 138, p. 83-105.

Holst, T. B., and Fossen, H., 1987, Strain distribution in a fold in the West Norwegian Caledonides: Journal of structural geology, v. 9, no. 8, p. 915-924.

Holtzman B. K., Kohlstedt, D. L., Zimmerman, M. E., Heidelbach, F., Hiraga, K.,

Hustoft, J., 2003, Melt segregation and strain partitioning: implications for seismic anisotropy and mantle flow: Science, v. 301, p. 1227–30.

Johnston, M. R., 1982, Sheet M28BD – Red Hills: Department of Scientific and Industrial Research, 1990, Geology of the St. Arnaud District, Southeast Nelson (sheet N29), 119.

Jung, H., Katayama, I., Jiang, Z., Hiraga, T., and Karato, S. I., 2006, Effect of water and stress on the lattice-preferred orientation of olivine: Tectonophysics, v. 421, no. 1, p. 1-22.

Kaplanis, A., Koukouvelas, I., Xypolias, P., and Kokkalas, S., 2013, Kinematics and Ophiolite obduction in the Gerania and Helicon Mountains, central Greece: Tectonophysics, v. 595, p. 215-234.

Karato, S., Jung, H., Katayama, I., and Skemer, P., 2008, Geodynamic significance of

seismic anisotropy of upper mantle: new insights from laboratory studies: Earth Planetary Sciences, v. 36, p. 59-95.

Katayama, I., Jung, H., and Karato, S., 2004, New type of olivine fabric from deformation experiments at modest water content and low stress: Geology, v. 32, no. 12, p. 1045-1048.

Kimura, J.-I., and Sano, S., 2012, Reactive melt flow as the origin of residual mantle lithologies and basalt chemistries in mid-ocean ridges: Implications from the Red Hills peridotite, New Zealand: Journal of Petrology, v. 53, no. 8, p. 1637-1671.

Kirby, S. H., and Green, H.W.II., 1980, Dunite xenoliths from Hualalai volcano: evidence for mantle diapiric flow beneath the island of Hawaii. Am. J. Sci., 280A: 550-575.

Lister, G.S., and Hobbs, B.E., 1980, The simulation of fabric development during plastic deformation and its application to quartzite: the influence of deformation history. Journal of Structural Geology, v. 2, p. 355-370.

Llana-Fúnez, S., and Rutter, E.H., 2014, Effect of strain geometry on the petrophysical properties of plastically deformed aggregates: experiments on Solnhofen limestone, *in* Llana-Fúnez, S., Marcos, A., and Bastida, F., eds., Deformation Structures and Processes within the Continental Crust: London, Geological Society [London] Special Publication, v. 394, p. 167–187.

Lloyd, G. E, Butler, R.H.W., Casey, M., Tatham, D.J., and Mainprice, D., 2011, Constraints on the seismic properties of the middle and lower continental crust, *in* Prior, D.J., Rutter, E.H., and Tatham, D.J., eds., Deformation Mechanisms,

Rheology and Tectonics: Microstructures, Mechanics and Anisotropy: London, Geological Society [London] Special Publication, v. 360, p. 226 7–32.

Michibayashi, K., Ina, T., Kanagawa, K., 2006, The effect of dynamic recrystallization on olivine fabric seismic anisotropy: Insight from a ductile shear zone, Oman ophiolite: Earth and Planetary Science Letters, v. 244, p. 695-708.

Miyazaki, T., Sueyoshi, K., and Hiraga, T., 2013, Olivine crystals align during diffusion creep of Earth/'s upper mantle: Nature, v. 502, p. 321-326.

Nicolas, A., and Christensen, N. I., 1987, Formation of anisotropy in upper mantle peridotites—a review. In: Fuchs, K., Froideoaux, C. (Eds.), Composition, Structure and Dynamics of the Lithosphere–Asthenosphere System. Trans. Ed. AGU, Washington, D.C., v. 16, p. 407–433.

Niu, Y., 1997, Mantle melting and melt extraction processes beneath ocean ridges: evidence from abyssal peridotites: J Petro, v. 38, p. 1047–1074.

Ozawa, K., 1989, Stress-induced Al-Cr zoning of spinel in deformed peridotites: Nature, v. 338, p. 141–144.

Casado, B. O., Gebauer, D., Schäfer, H. J., Ibarguchi, J. G., and Peucat, J. J., 2001, A single Devonian subduction event for the HP/HT metamorphism of the Cabo Ortegal complex within the Iberian Massif: Tectonophysics, v. 332, no. 3, p. 359-385.

Passchier, C. W., and Trouw, R.A., 2005, Microtectonics, Germany, Springer.

Pfiffner, O. A., and Ramsay, J. G., 1982, Constraints on geological strain rates:

arguments from finite strain states of naturally deformed rocks: Journal of Geophysical Research: Solid Earth (1978–2012), 87(B1), 311-321.

Poli, L. C., and Oliver, G. J. H., 2001, Constrictional deformation in the Central Zone of the Damara Orogen, Namibia: Journal of African Earth Sciences, v. 33, no. 2, p. 303-321.

Ramsay, J.G., and Huber, M.I., 1983, The Techniques of modern structural geology: San Diego, Academic Press, 307.

Ribe, N.M., and Yu, Y., 1991, A theory for plastic deformation and textural evolution of olivine polycrystals: Journal of Geophysical Research, v. 96, p. 8325–8335.

Sano, S., and Kimura, J. I., 2007, Clinopyroxene REE Geochemistry of the Red Hills Peridotite, New Zealand: Interpretation of Magmatic Processes in the Upper Mantle and in the Moho Transition Zone: Journal of Petrology, v. 48, no. 1, p. 113-139.

Schmid, S.M., and Casey, M., 1986, Complete fabric analysis of some commonly observed quartz c-axis patterns. American Geophysical Union Geophysical Monograph, v. 36, p. 263-286.

Secher, D., 1981, Les lherzolites ophiolitiques de Nouvelle-Caledonie et leurs gisements de chromite − deformation de la chromite. Unpublished 3me cycle thesis, University of Nantes.

Shervais, J. W., 2001, Birth, death, and resurrection; the life cycle of suprasubduction zone ophiolites: Geochemistry, Geophysics, Geosystems, v. 2, no. 1, p. 45.

Skemer, P., Warren, J.M., and Kelemen, P. B., 2010, Microstructural and rheological

evolution of a mantles shear zone: J.Petrol. v. 51 no. 1–2, p. 43–53.

Solar, G. S., and Brown, M., 2001, Petrogenesis of migmatites in Maine, USA: possible source of peraluminous leucogranite in plutons? Journal of Petrology, v. 42, no. 4, p. 789-823.

Soustelle, V., Tommasi, A., Demouchy, S., and Ionov, D. A., 2010, Deformation and fluid-rock interaction in the supra-subduction mantle: Microstructures and water contents in peridotite xenoliths from the Avacha Volcano, Kamchatka: Journal of Petrology, v. 51, no. 1-2, p. 363-394.

Stewart, E., 2015, The structural and petrologic evolution of the upper mantle during subduction-initation (Doctoral dissertation, Texas A&M University).

Sullivan, S. E., and Arthur, M. B., 2006, The evolution of the boundary less career concept: Examining physical and psychological mobility: Journal of Vocational Behavior, v. 69, no. 1, p. 19-29.

Sullivan, W.A., and Beane, R.J., 2010, Asymmetrical quartz crystallographic fabrics produced during constrictional deformation: Journal of Structural Geology, v. 32, p. 1430-1443.

Sullivan, W. A., 2013, L tectonites: Journal of Structural Geology, v. 50, p. 161-175.

Sylvester, A. G., and Janecky, D. R., 1988, Structure and petrofabrics of quartzite and elongate pebbles at Sandviksfjell, Bergen, Norway: Norsk geologisk tidsskrift, v. 68, no. 1, p. 31-50.

Tommasi, A., Tikoff, B., and Vauchez, A., 1999, Upper mantle tectonics: three-

dimensional deformation, olivine crystallographic fabrics and seismic properties: Earth and Planetary Science Letters, v. 168, p. 173-186.

Tullis, J., 1977, Preferred orientation of quartz produced by slip during plane strain: Tectonophysics, v. 39, no. 1, p. 87-102.

Underwood, E. E., 1970, Quantitative stereology, Addison-Wesley Publishing Company.

Van der Wal, D., Chopra, P., Drury, M., and Gerald, J. F., 1993, Relationships between dynamically recrystallized grain size and deformation conditions in experimentally deformed olivine rocks: Geopyhysical Research Letters, v. 20, no. 14, p. 1479-1482.

Walcott, R. I., 1969, Geology of the Red Hill complex, Nelson, New Zealand: Transactions of the Royal Society of New Zealand, v. 7, no. 5, p. 57-88.

Warren, J. M., and Hirth, G., 2006, Grain size sensitive deformation mechanisms in naturally deformed peridotites: Earth and Planetary Science Letters, v. 248, p. 438-450.

Warren, J. M., Hirth, G., and Kelemen, P. B., 2008, Evolution of olivine lattice preferred orientation during simple shear in the mantle: Earth and Planetary Science Letters, v. 272, no. 3, p. 501-512.

Zhang, S., and Karato, S., 1995, Lattice preferred orientation of olivine aggregates deformed in simple shear: Nature, v. 375, p. 774–777.

Zhang, S., Karato., S., Fitzgerald, J., Faul, U.H., and Zhou, Y., 2000, Simple shear deformation of olivine aggregates: Tectonophysics, v. 316, no. 1-2, p. 133-152.

APPENDIX A

FIGURES
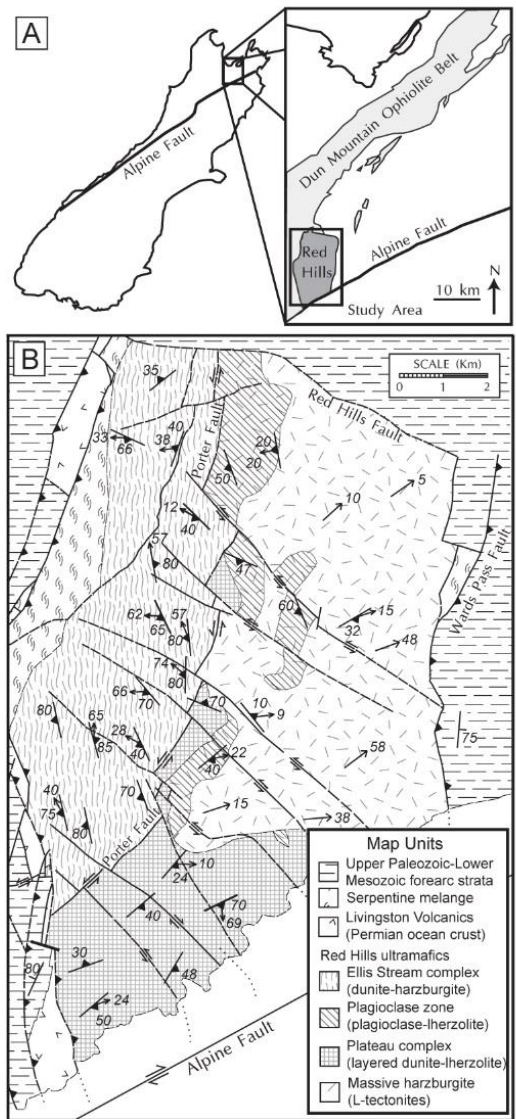
**Figure 1**: a) Map showing the Red Hills location in the Dun Mountain Ophiolite Belt of New Zealand and b) the location of the Red Hills rocks analyzed in this study (Stewart, 2015).
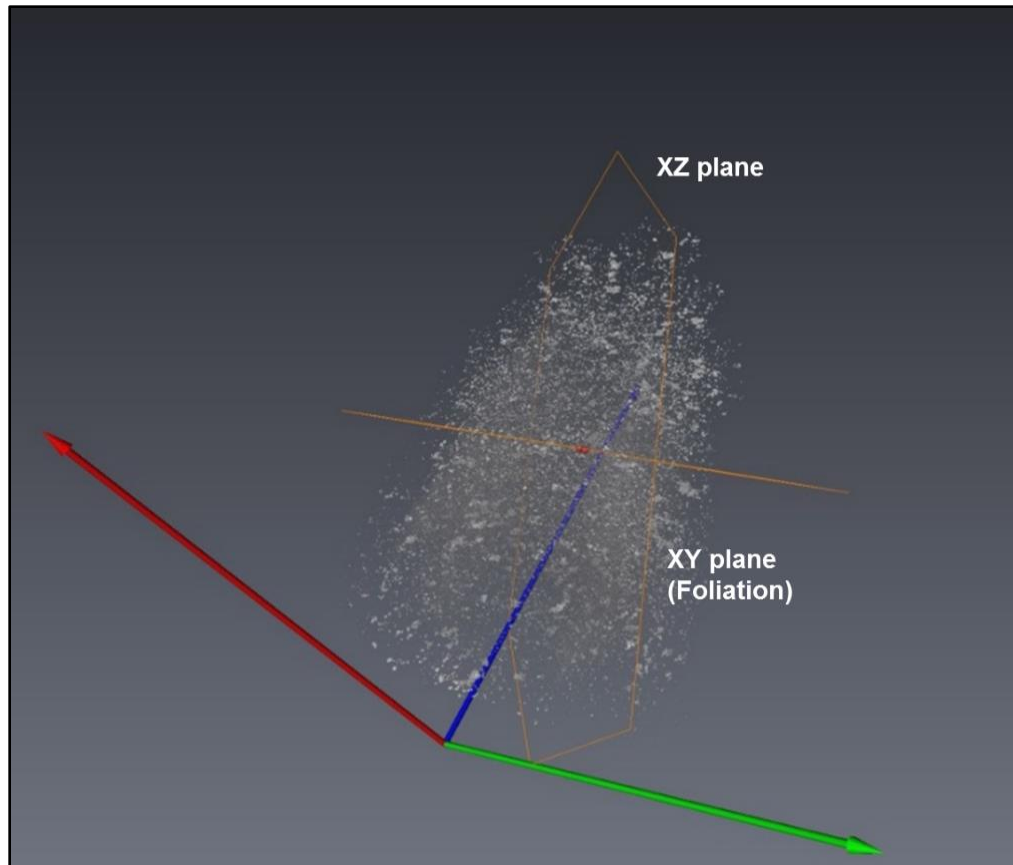
31
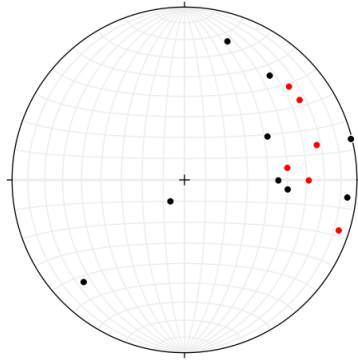
**Lineation**                    **Foliation**
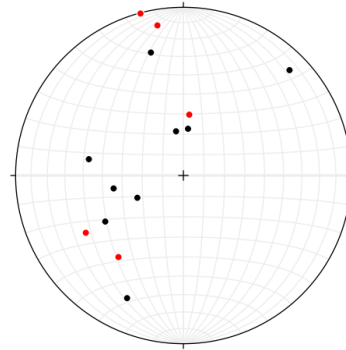


●    **This study**

●    **Field data (Stewart, 2015)**

**Figure 2:** Equal area, lower hemisphere projection of foliation and lineation. Black dots denote orientations derived from this study from X-ray CT analysis and lineation is defined by long axis of spinel. Red dots represent orientation data taken in the field (Stewart, 2015).

**Figure 3:** Grey pixels are spinel grains produced using the X-ray CT. The XY plane (foliation) and XZ plane are shown. The intersection of the XY and XZ plane defines the lineation.
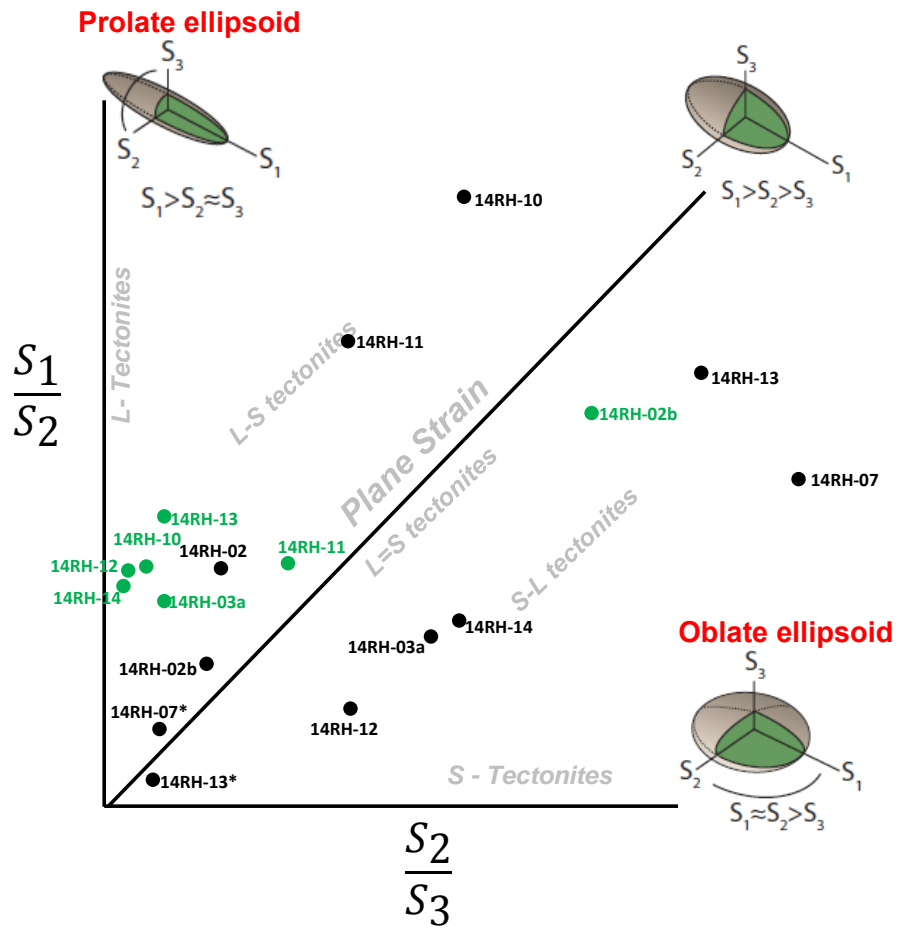
**Figure 4:** Flinn diagram; $S_1$, $S_2$, and $S_3$ are the maximum, intermediate, and minimum axes of the finite strain ellipsoid, respectively. Olivine (green dots) 3D fabric shape was derived from grain tracing and Image SXM, and spinel (black dots) 3D fabric shape was derived from the X-ray CT. * indicates results from smaller samples (14RH-13* and 14RH-07*) Ellipsoids from Chatzaras and Kruckenberg (in review).
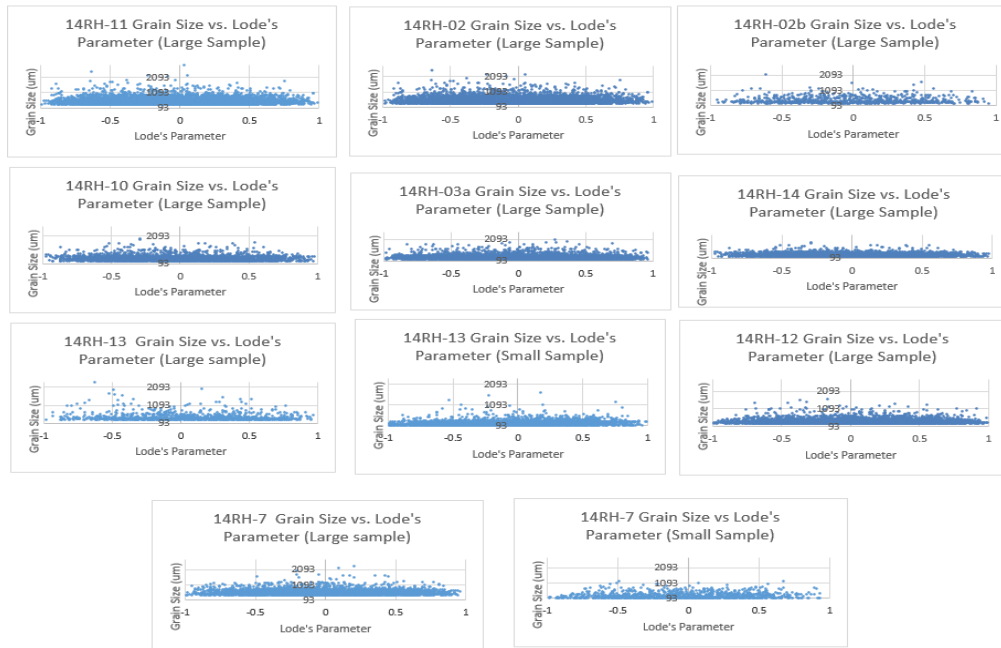
**Figure 5:** Lode's parameter derived from X-ray CT data for each individual spinel grain analyzed. Data is shown for both large and small samples.
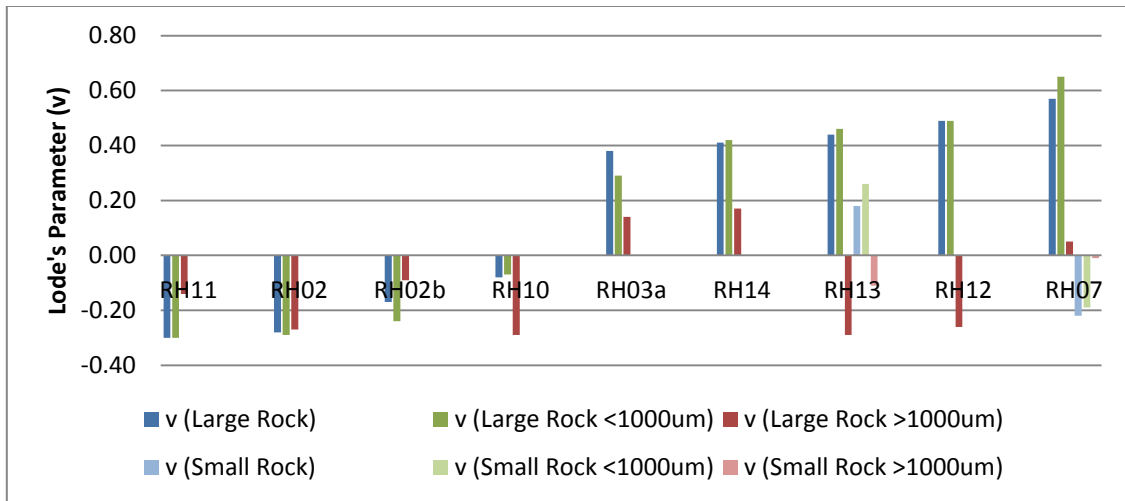
**Figure 6:** Lode's parameter derived from X-ray CT data for three different grain size populations: (1) all spinel grains, (2) all spinel grains < 1000 μm, and (3) all spinel grains > 1000 μm. Lode's parameter vs. grain size is also provided for the two smaller samples (shown as lighter shades for samples 14RH-07 and 14RH-13).
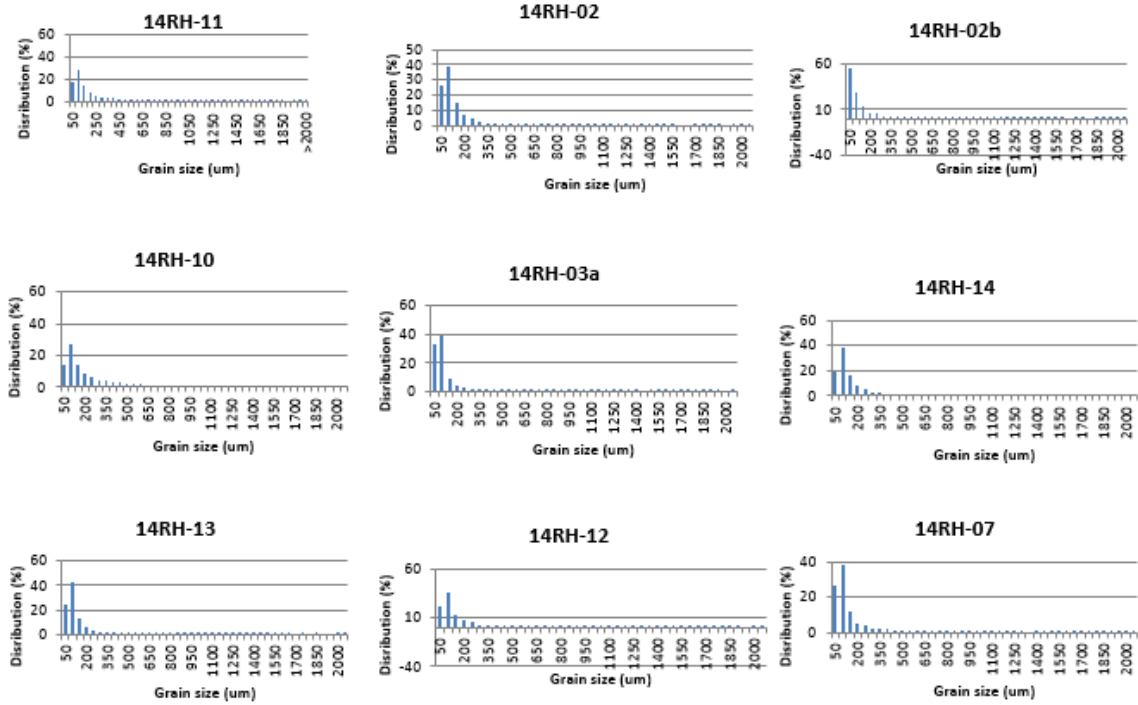
**Figure 7:** Grain size distributions for all samples. Grain sizes range from 30 to 5000 µm (cutoff of 30 µm used due to resolution of the EBSD).
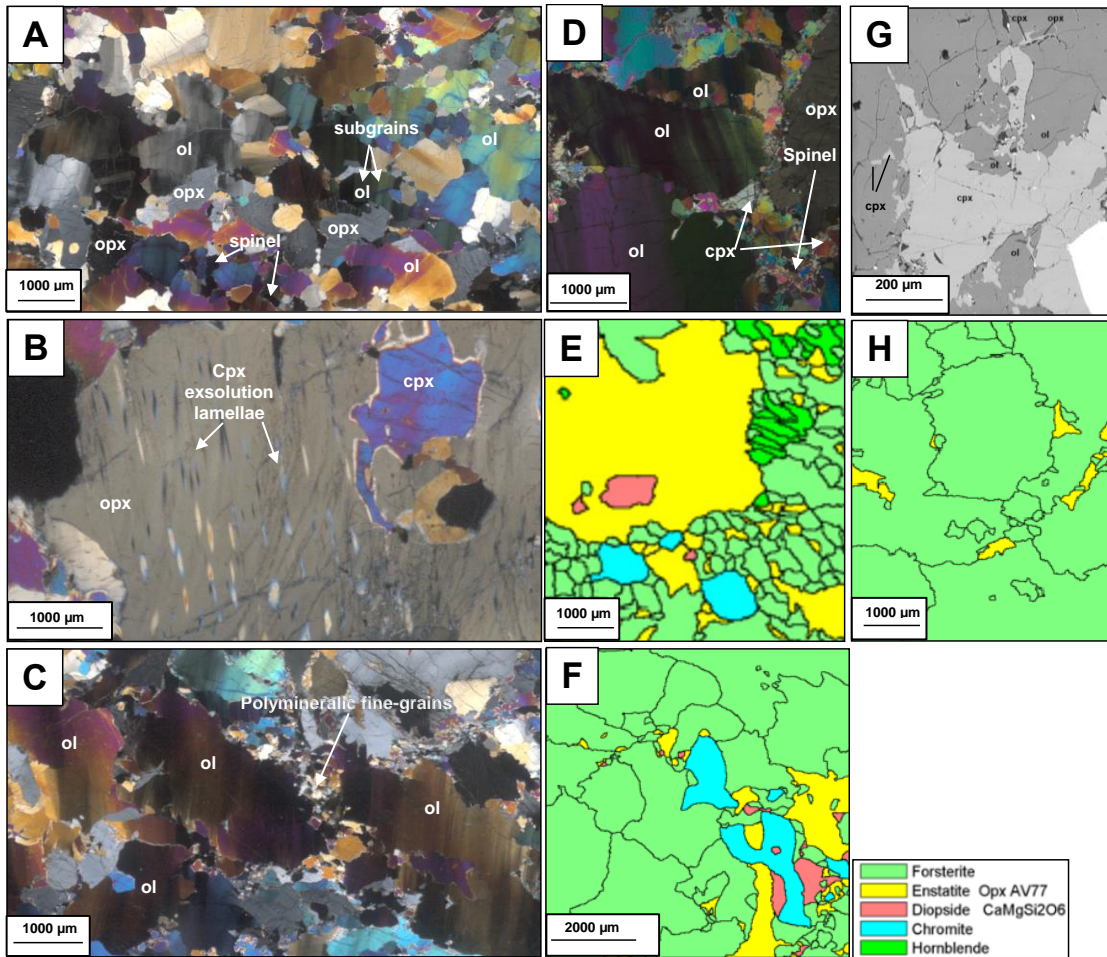
**Figure 8:** Cross polarized optical microscope image (A-D); EBSD phase maps (E, F, H) backscatter electron image (G). A) Sample 14RH-11 showing a distribution of olivine, orthopyroxene, spinel, and clinopyroxene. Olivine grains show undulatory extinction and subgrains. B) 14RH-12 with large grains of orthopyroxene grains containing exsolution lamellae of clinopyroxene. C) 14RH-13 with a fine-grained, polymineralic composition in between coarse-grained olivine with a similar orientation and size. D) Fine-grained clinopyroxene and olivine surround larger grains of orthopyroxene and olivine. E) 14RH-14 with large orthopyroxene grains surrounded by finer-grained olivine F) 14RH-11 showing coarse-grained spinel with curved and irregular grain boundaries. G) 14RH-03b showing fine-grained clinopyroxene surrounding olivine and coarse grained clinopyroxene. Spinel grain is white. H) 14RH-12 showing fine-grained orthopyroxene proximal to coarse- grained olivine.
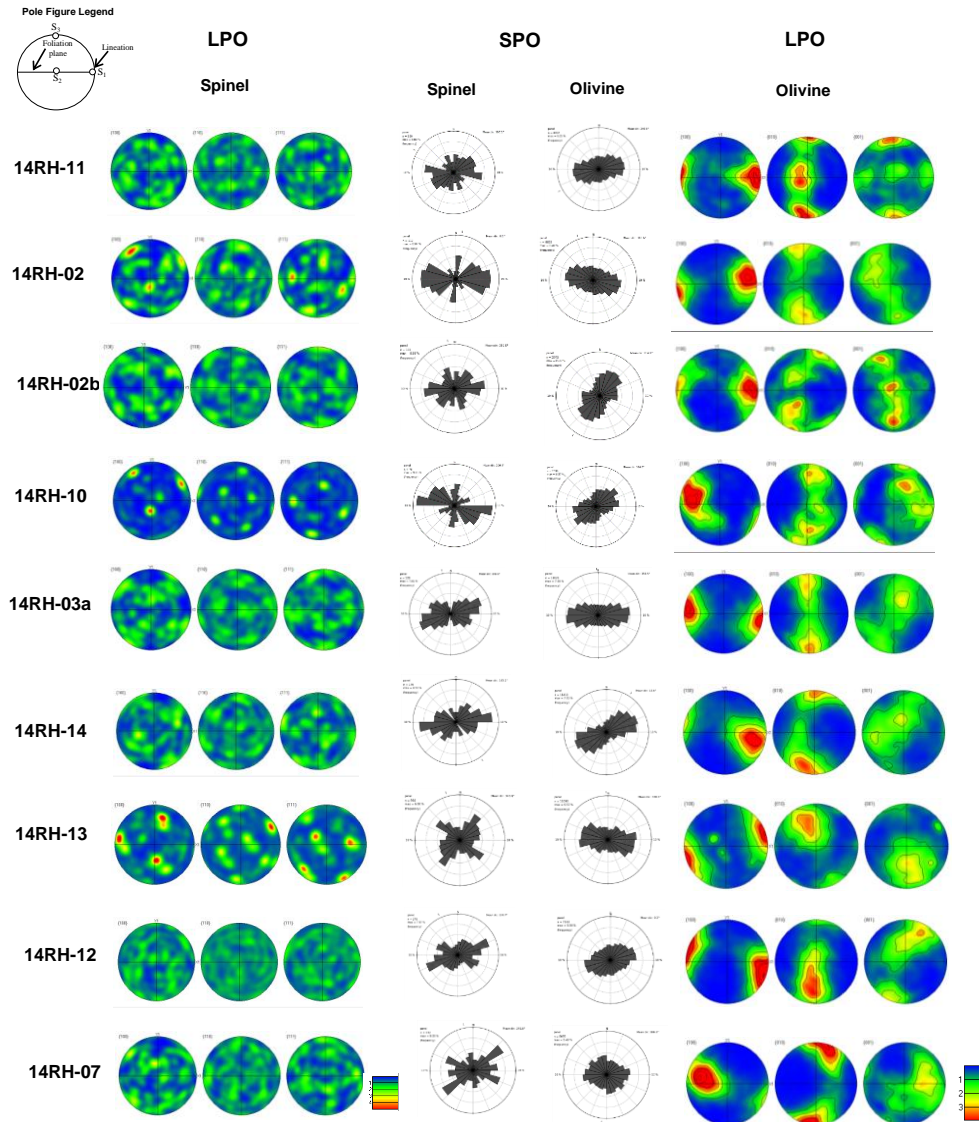
**Figure 9:** Olivine and Spinel LPO for whole rock samples. Data is shown as lower hemisphere, equal area stereographic projections. Foliation is the E-W diameter and the lineation is horizontal within that plane. For spinel LPO, the poles to {010}, {001}, and {100} are shown and for olivine, the poles to {100}, {010} and {001} are shown. Rose diagrams of olivine and spinel SPO are shown relative to the average SPO of spinel defined by the X-ray CT. Pole figure legend includes the location of the foliation plane, lineation, and S1, S2, and S3 are the maximum, intermediate, and minimum principal strain axes, respectively.
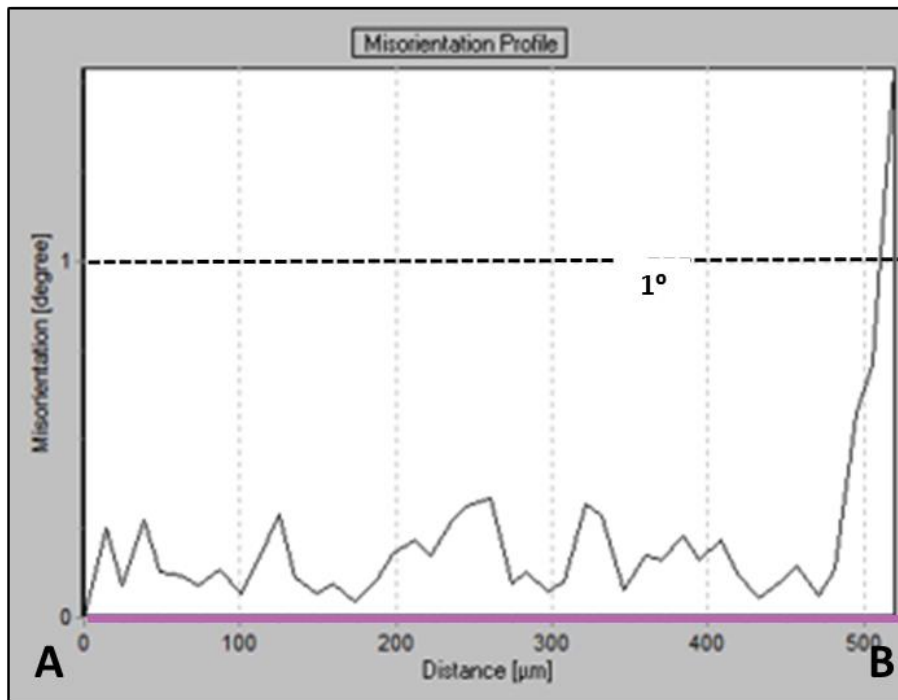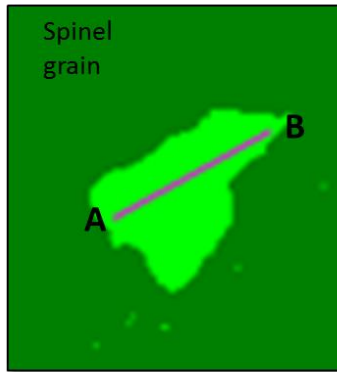
**Figure 10:** EBSD phase map showing a spinel grain with a transect from A to B and the Misorientation profile below. All Misorientation falls below one degree.
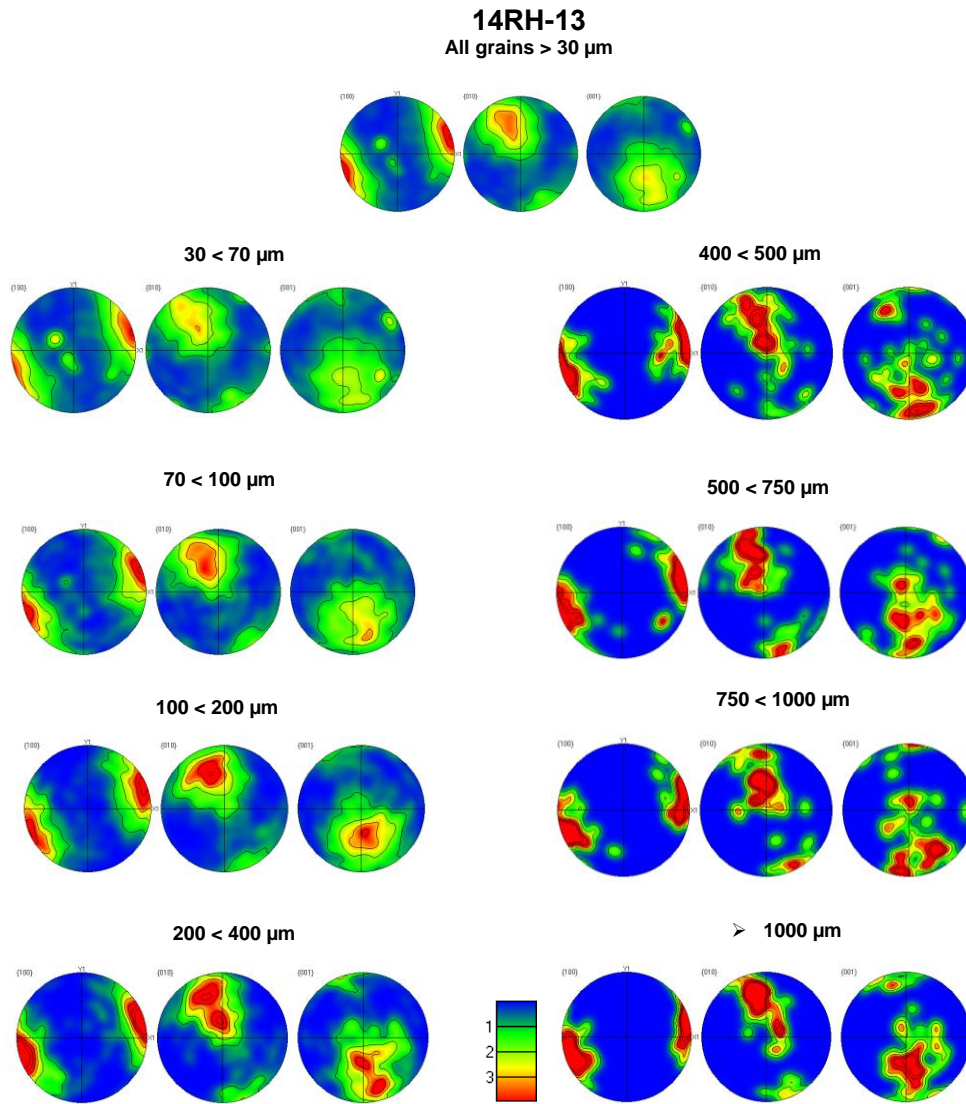
**Figure 11:** Olivine LPO for sample 14RH-13 presented for multiple grain size populations. The LPO does not appear to change with respect to which grain size population is evaluated. This analysis was performed for all samples, and this dataset is representative of the average trend derived for each sample.
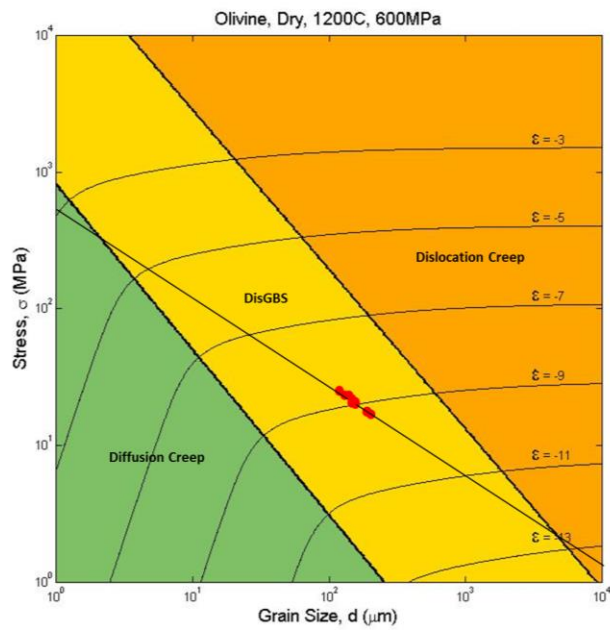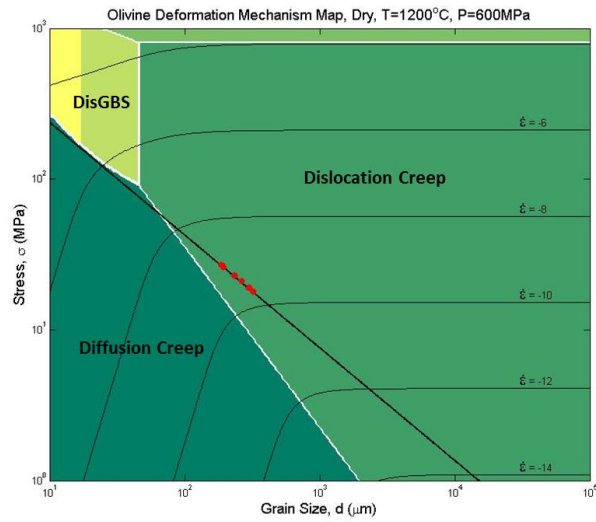
**Figure 12:** Deformation mechanism map for dry olivine at 1200ºC and 600 MPA created using variables from Hirth and Kohlstedt (2003) on the left and Hansen et al. (2011) on the right with stress piezometer (black line) superimposed (Van der Waal et al., 1993). Mean grain size used for olivine, excluding grains <30 μm, was derived from EBSD data for each sample.

APPENDIX B

TABLES

**Table 1**
**Modal**
**Mineralogy**

| Sample No. | Olivine | Orthopyroxene | Clinopyroxene | Spinel | Pyrope | Anorthite | Hornblende |
|---|---|---|---|---|---|---|---|
| 14RH11 | 52.79% | 27.79% | 17.85% | 1.56% | 0.00% | 0.00% | 0.00% |
| 14RH02 | 77% | 16.32% | 2.97% | 0.01% | 0.01148% | 0.0002938% | 0.2584% |
| 14RH02b | 85.70% | 11.90% | 2.05% | 0.34% | 0.00% | 0.00% | 0.00% |
| 14RH10 | 76% | 20.40% | 2.96% | 0.60% | 0.00% | 0.00% | 0.00% |
| 14RH03a | 81% | 14.30% | 4.44% | 0.24% | 0.00% | 0.00% | 0.00% |
| 14RH14 | 73.35% | 18.19% | 6.31% | 0.43% | 0.07% | 0.00% | 1.65% |
| 14RH13 | 37% | 12.44% | 13.70% | 2.96% | 0.2101% | 0.061% | 33.22% |
| 14RH12 | 51% | 26.22% | 18.26% | 1.86% | 0.056670% | 0.00% | 2.15% |
| 14RH07 | 74% | 20.68% | 2.17% | 0.1758% | 0.005206% | 0.0003045% | 0.2516% |

*Remainders are fractured or serpentinized areas.